JOURNAL OF PROPULSION AND POWER
Vol. 17, No. 2, March–April 2001

Upstream-Propagating Potential Disturbances in the F109 Turbofan Engine Inlet Flow

Eric A. Falk* and Eric J. Jumper†
University of Notre Dame, Notre Dame, Indiana 46556
and
Michael K. Fabian‡ and Jerry Stermer§
U.S. Air Force Academy, Colorado Springs, Colorado 80840

An experimental investigation of the unsteady-velocity field upstream of the single-stage axial fan in a F109 turbofan engine was performed. Phase-locked, three-component velocity measurements were collected at multiple axial, radial, and azimuthal locations directly forward of the fan, out to 1.0 fan-blade chords upstream. The measured velocity data were ensemble averaged and resolved into mean and unsteady components, where the unsteady components were further decomposed into elements of amplitude, frequency, and phase for the primary and first-harmonic frequencies. Analysis of the primary-frequency phase information demonstrated the measured unsteady velocities to be potential in nature, generated by the fan, and to propagate upstream at acoustic speeds into the engine inlet flow. Furthermore, the axial component of the unsteady velocity data was found to exhibit peak-to-peak fluctuations of nearly 20% of the mean-axial velocity very near the fan, whereas the azimuthal (swirl) component exhibited fluctuations reaching nearly 50% of the mean-axial velocity at the same measurement locations. A computational simulation of the velocity field upstream of the F109 fan demonstrated good quantitative agreement with the measured unsteady velocity amplitudes.

Nomenclature

A = amplitude
a = speed of sound
c = fan-blade chord
d = fan rotation distance
e = root-mean-square error
f = frequency
t = time
U = velocity
x = Cartesian coordinate
y = Cartesian coordinate
z = Cartesian coordinate
Δ = incremental distance
η = disturbance-propagation angle
θ = azimuthal position
φ = disturbance phase

Subscripts

c = compressible component
h = harmonic-frequency component
i = incompressible component
p = primary-frequency component
R = radial component
x = x-coordinate component
y = y-coordinate component
z = z-coordinate component
θ = azimuthal component

Superscripts

$'$ = unsteady component
$\bar{}$ = mean component

Received 4 September 1999; revision received 30 June 2000; accepted for publication 15 July 2000.

*Graduate Research Assistant, Department of Aerospace and Mechanical Engineering, Hessert Center for Aerospace Research. Student Member AIAA.

†Professor, Department of Aerospace and Mechanical Engineering, Hessert Center for Aerospace Research. Associate Fellow AIAA.

‡Assistant Professor, Department of Aeronautics, Headquarters, U.S. Air Force Academy, Dean of Faculty, Department of Aeronautics. Member AIAA.

§Director of Test Cell Operations, Headquarters, U.S. Air Force Academy, Dean of Faculty, Department of Aeronautics.

Introduction

UNSTEADY aerodynamic forcing is known to play a significant role in producing structural high-cycle-fatigue (HCF) within turbomachine compressor blades and vanes. Traditionally, such forcing has been considered to be primarily composed of downstream-propagating vortical disturbances, created by the viscous wakes developed from upstream blade/vane components. These vortical disturbances convect with the mean flow, eliciting an unsteady structural response from the downstream components they encounter. Purely vortical forcing, however, does not provide a complete representation of the compressor forcing environment because unpredicted HCF failures continue to occur in modern compressors.[1] In fact, recent investigations have shown that other, previously unaccounted for, forcing mechanisms may also contribute to compressor HCF failure. In particular, the compressor forcing environment also includes propagating, unsteady potential disturbances, especially, as will be emphasized here, upstream-propagating potential disturbances elicited by downstream blade/vane components.

Potential disturbances are inviscid perturbations generated by the existence of a structural member, such as a blade/vane component, in the flow. At subsonic speeds, these disturbances propagate acoustically both upstream and downstream, and their strength decays with distance.[2] Because of their decay characteristics and high propagation speeds, the role of potential disturbances in aerodynamic forcing has historically been considered second order; particularly when compared to slower-propagating, viscously dissipated vortical disturbances. However, as engine through-flow speeds have increased and compressor stage-to-stage separation has decreased, potential disturbances have begun to be recognized as first-order factors in HCF production.[2]

Recent investigations examining the effects of potential forcing in turbomachine flows have reported important computational and experimental results. For example, by solving the unsteady isentropic Euler equations, Lewis et al.[3] were able to compute the potential

forcing on an upstream vane due to a downstream blade, finding the forcing to produce significant, unsteady, vane surface-pressure response, especially near the trailing edge. Additionally, Manwaring and Wisler[4] and Feirerisen and Fleeter[5] each successfully formulated analytical methods to decouple interacting vortical and potential disturbances present in velocity data collected downstream of low-speed compressor-rig blade rows. Their studies showed the necessity of including potential disturbances in forcing models[4] because similar-order potential and vortical disturbances combined to produce the overall unsteady aerodynamic field.[5]

Johnston and Fleeter[6,7] experimentally measured the unsteady velocity field between an inlet-guide-vane (IGV) row and a high-speed research fan, and showed the IGV wake character to be altered by the upstream-propagating rotor potential disturbances. Hsu and Wo[8] similarly examined the unsteady velocity field between rotor/stator rows in a low-speed compressor rig, and concluded that upstream-propagating stator potential disturbances could modify the measured downstream-propagating rotor wakes, dependent on the rotor/stator spacing. Additionally, Probasco et al.,[9,10] Fabian and Jumper,[11] and Fabian et al.[12] all experimentally investigated the effect of upstream-propagating potential forcing on vane surface-pressure response. Their studies independently found the vane surface-pressure response, induced by potential forcing, to be significant, particularly near the vane trailing edge.[12] Fabian et al. further showed the vane surface-pressure response to the upstream-propagating potential forcing to be on the same order of magnitude as that induced by downstream-propagating vortical and potential disturbances.[12]

Clearly, the aforementioned investigations demonstrate potential forcing to play a significant role in comprising the total unsteady-velocity field, and unsteady component response, within a turbomachine compressor. This appears to be particularly accurate in the case of upstream-propagating potential disturbances, where such disturbances cannot only modify an incoming disturbance field, but also substantially affect the surface-pressure response of an upstream blade/vane component. Unfortunately, the previous conclusions regarding potential forcing have been drawn almost exclusively from computational studies or experiments in idealized compressor rigs and cascades. Few, if any, previous potential-forcing investigations have been performed in an actual aircraft engine. Moreover, none of the previous studies have isolated and directly measured an upstream-propagating potential field, which relegated their results to the description of potential-disturbance effects rather than the disturbances themselves. The purpose of the present study, therefore, is to measured and characterize isolated, upstream-propagating potential disturbances forward of a high-speed turbofan engine fan, thereby providing information from which future unsteady-forcing investigations can more accurately describe wake interactions and component surface-pressure response due to potential forcing.

Facilities and Equipment

The Honeywell (AlliedSignal) F109 turbofan engine, located in engine test cell 3 at the U.S. Air Force Academy in Colorado Springs, Colorado, was modified to accommodate the data acquisition equipment for this study. The F109 has a single stage of axial compression, as shown in Fig. 1, with no existing flow perturbations (i.e., IGV stage, etc.) forward of the fan. A bell-mouth inlet screen (normally in place to prevent foreign object ingestion) was removed from the F109 to allow for instrumentation. As shown schematically in Fig. 2, a probe arm, aerodynamic fairing, and TSI 9400 XYZ mirror-mount traverse were integrated into the engine test facility as positioning tools for a TSI 1247A-10 miniature cross-flow hot-film X probe, which was mounted to the end of the probe arm. The traverse rested on a rolling platform hard mounted to the engine; thus, engine movement during testing, due to thrust, was concomitantly experienced by the traverse. This assembly allowed for positioning of the X probe in the bell mouth without flow contamination of the engine inflow (see Ref. 13 for further details).

The X probe could be mounted vertically for $x-y$ plane measurements, as shown in Fig. 2, or rotated 90 deg from vertical for $x-z$ plane measurements. The probe had a full range of movement in all

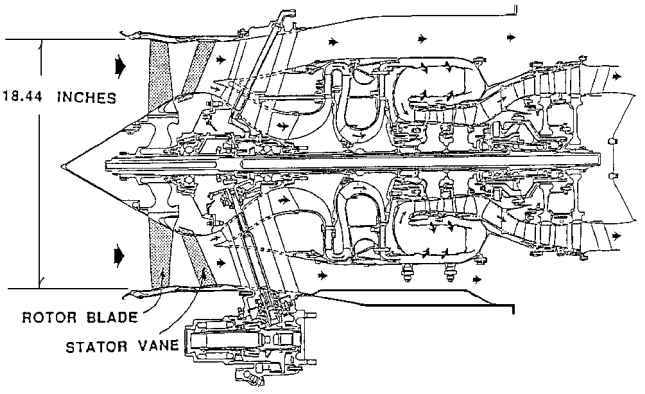

Fig. 1 Cutaway view of the Honeywell F109 turbofan engine.

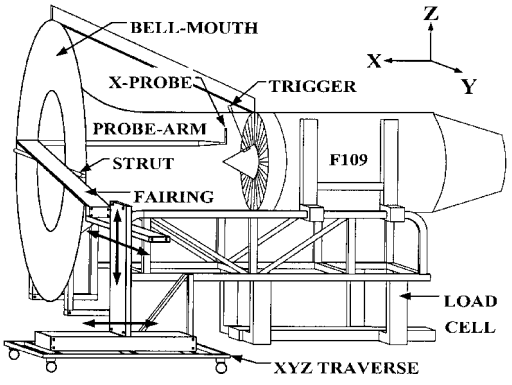

Fig. 2 Perspective view of the U.S. Air Force Academy F109 turbofan engine.

three coordinate directions, depicted in Fig. 2, with movements as small as 0.01 mm possible (all distances reported here are accurate to ± 0.01 mm). Axial X-probe positions reached within 12.70 mm of the fan face, where the fan chord was 63.50 mm at the given radial measurement locations. Portions of the data presented here are reported much closer to the fan than 12.70 mm. These data were acquired before the implementation of traverse safety mechanisms.

A TSI IFA-100 thermal anemometry system was used for the hot-film velocity measurements, where the hot-film anemometer had a calibrated frequency response of ~80 kHz. A Compaq Deskpro 4/33i computer and its associated software were used for traverse positioning. The data acquisition equipment consisted of an RC Electronics ICS-16E data acquisition card housed in a GTSI DeskTop 100-MHz computer. Steady-state, engine-diagnostic data, including inlet-flow temperature and fan revolutions per minute (rpm), were acquired via a Hewlett Packard 3852A data acquisition system using existing instrumentation on the engine. A Keyence FS2-65 photoelectric sensor allowed for phase-locked data acquisition.

Scope of Testing

Velocity measurements were made along four axial engine rays, where an engine ray is defined as a line parallel to the longitudinal axis of the engine, as shown schematically in Fig. 3. Along each engine ray, nine data-collection locations were axially spaced in increments of $0.10c$, or 6.35 mm, with the data-collection location nearest the fan located at $x/c = 0.20$ (where x is measured as shown in Fig. 3). The four engine rays were azimuthally aligned such that the position of two rays coincided with the leading-edge location of a stator vane aft of the fan, denoted vane B in Fig. 4. The azimuthal position of the other two engine rays coincided with the center of a stator spacing, denoted vane AB in Fig. 4. The rays were positioned along two radial locations, engine axis 1 (EA 1) and engine axis 2 (EA 2), as shown in Figs. 3 and 4. EA 1 corresponded to a radial distance of 218.0 mm from the centerline of the engine, whereas EA 2 corresponded to a radial distance of 205.0 mm from

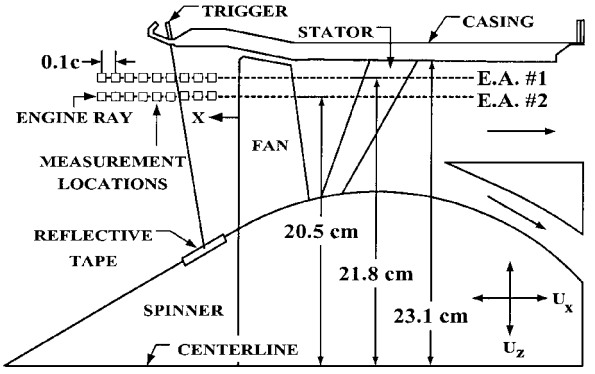

Fig. 3 Side view of F109 compressor section, with measurement locations shown.

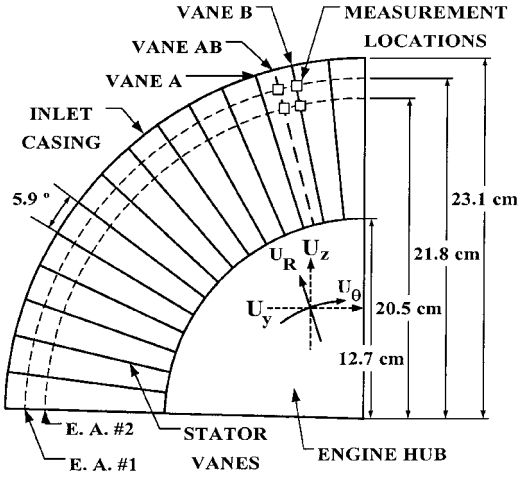

Fig. 4 Front view of F109 stator-vane row, with measurement locations shown.

the engine centerline. The inner radius of the engine inlet shroud was 231.0 mm.

Velocity data were acquired at all EA 2 locations in both the $x-y$ plane and $x-z$ plane probe orientations. In the $x-y$ plane orientation, the X probe measured U_x and U_y velocity components. In the $x-z$ plane orientation, the X probe measured U_x and U_z velocity components, where the U_x, U_y, and U_z velocity components correspond to the directions shown in Figs. 3 and 4. Because of space limitations within the bell mouth, only $x-y$ plane velocity data were acquired at the EA 1 radial location.

Phase locking of the data was accomplished via a photoelectric sensor, or trigger. Data acquisition was initiated when the trigger transmitted a single voltage spike as it received reflected light from a piece of retroreflective tape permanently bonded to the engine spinner, as shown schematically in Fig. 3. Once triggered, a single set of hot-film voltage data was acquired using software developed to collect 1024 data samples on four channels, 256 per channel, at a sequential acquisition rate of 1.0 MHz, or 250 KHz per channel. A total of 200 data sets were collected at each measurement location and fan rpm. Three fan rpm were examined: 12,050, 13,300, and 14,375 fan rpm, corresponding to 90, 94, and 98% engine speed, respectively.

Data Treatment

Ensemble Averaging

The 200, phase-locked voltage sets acquired at each data collection location and fan rpm were ensemble averaged. Representative results of collecting fewer than 200 sets at a given location are shown in Fig. 5 for the U_x velocity, 13,300 fan rpm, EA 2, vane B, $x/c = 0.10$ location. In Fig. 5, it is evident that the averaging process removed much of the higher-order frequency content from the single set, while also reducing its peak-to-peak velocity amplitude due to slight phase variations between sets. However, the rms fluctuation of the single set was not significantly reduced (~3%) by the averaging, and, more important, the phase of the primary frequency was well preserved throughout the process.

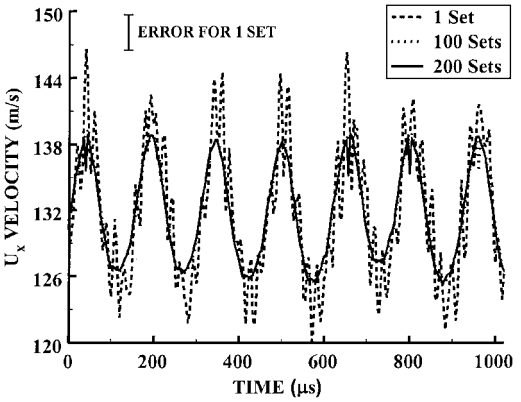

Fig. 5 Comparison between 1-ensemble, 100-ensemble, and 200-ensemble sets.

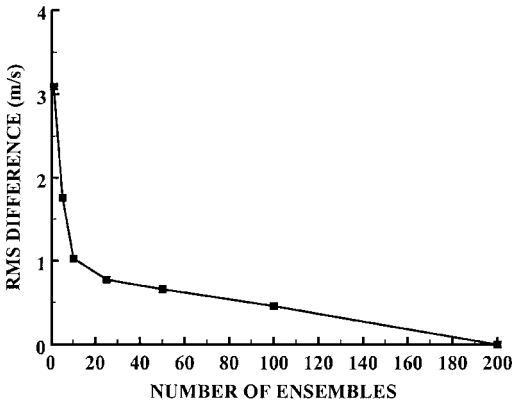

Fig. 6 Lesser-ensemble sets vs 200-ensemble set, rms velocity difference.

Comparison of the 100- and 200-ensemble sets in Fig. 5 reveals few differences. Figure 6 shows the rms velocity difference between lesser-ensemble sets and the 200-ensemble set of Fig. 5. From Fig. 6 it is evident that the rms difference decreases rapidly with increasing sets; the difference between 10 and 200 ensembles is only ~1.0 m/s [the mean-axial velocity (MAV) was ~100 m/s]. Moreover, given the approximate convergence of the rms velocity difference after 25 ensembles, the 200-ensemble set can be assumed to represent the true average signal, within the experimental error of the measurement (the difference between 200 and 400 ensembles was 0.21% of the MAV). Note that the error bars depicted in following figures of this paper indicate experimental error in the measured velocity data, as computed in Ref. 13.

Frequency Decomposition

The unsteady velocity data were decomposed into elements of amplitude, frequency, and phase, for the primary and first-harmonic (twice the primary) frequencies, through the optimization routine described in Ref. 13. This routine modeled the unsteady velocity data as a superposition of two sine waves, for the primary and first-harmonic frequency components, as given by

$$U' = A_p \sin(2\pi f_p t + \varphi_p) + A_h \sin(2\pi f_h t + \varphi_h) \qquad (1)$$

The routine varied the amplitude, frequency, and phase of the primary and first-harmonic components until the minimum rms error between Eq. (1) and the measured data was obtained. Representative results from this decomposition are presented in Table 1, for the U'_x velocity, 13,300 fan rpm, EA 2, vane B location.

Reconstruction of the decomposed velocity data could be performed through use of Eq. (1) and Table 1, where the reconstructed

Table 1 Decomposed data: U'_x velocity; 13,300 fan rpm; EA 2; vane B location

x/c	A_p, m/s	A_h, m/s	f_p, Hz	f_h, Hz	φ_p, rad	φ_h, rad	e, m/s
1.0	0.21	0.03	6,557	13,199	−1.93	−14.56	0.14
0.9	0.21	0.01	6,578	11,063	−1.86	−12.57	0.16
0.8	0.30	0.04	6,578	13,345	−1.59	−10.93	0.19
0.7	0.50	0.04	6,542	13,022	−1.24	−8.84	0.23
0.6	0.85	0.05	6,532	13,002	−0.78	−6.28	0.27
0.5	1.28	0.07	6,524	12,939	−0.29	−4.34	0.31
0.4	1.94	0.22	6,523	13,065	0.22	−0.16	0.35
0.3	2.81	0.39	6,532	13,061	0.81	−0.54	0.44
0.2	3.90	0.59	6,528	13,067	1.36	0.87	0.57

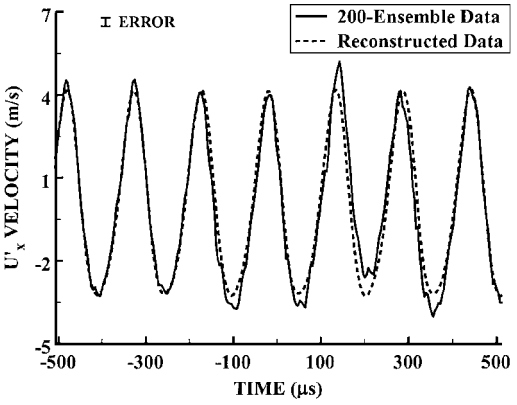

Fig. 7 Comparison between 200-ensemble data and reconstructed data.

U'_x velocity at $x/c = 0.20$ and its concomitant 200-ensemble set are given in Fig. 7. From Fig. 7 it is clear that the reconstructed data accurately reproduce the overall structure, frequency, and phase of the 200-ensemble set. Small differences are evident between the two data sets in Fig. 7; however, these differences are approximately within the experimental error of the measurement.[13] The agreement between the reconstructed and measured data sets in Fig. 7 is typical of the accuracy with which all of the reconstructed data represent the ensemble data collected during this investigation. Table 1 gives the rms error between the reconstructed and 200-ensemble data, which shows the rms error to be relatively small.

Note that the phase error of the data presented in this paper is directly attributable to both the rms error given in Table 1 and the experimental error. It is difficult, however, to compute the phase error from the rms error in Table 1 because phase error is essentially an error in the time axis. Similarly, the experimental phase error is also difficult to compute because slight phase variations occurred in each set comprising the 200 ensemble. However, if the 200 ensemble represents the true velocity waveform, as argued earlier, the phase error in the 200 ensemble will be negligible. As such, phase error will not be reported here; its omission does not affect the results of the subsequent analysis.

Coordinate Transformation

As mentioned earlier, two components of velocity were collected in both the x–y and x–z planes, allowing U_x to be measured in both planes. Figure 8 shows the 200-ensemble U'_x data obtained in both the x–y and x–z planes at 13,300 fan rpm, EA 2, vane B, $x/c = 0.3$. From Fig. 8, it is clear that the U'_x velocities have the same overall amplitude, frequency, and phase. Such good agreement between the U'_x velocities verifies that the x–y and x–z plane measurements were not contaminated by cross-flow components.

Because the velocity fields in both planes were measured at the same locations and phase locked, a conversion from Cartesian to cylindrical coordinates was possible. This conversion was performed via the following equation:

$$U_A = U_x, \qquad U_\theta = U_y \sin\theta - U_z \cos\theta$$
$$U_R = U_y \cos\theta + U_z \sin\theta \tag{2}$$

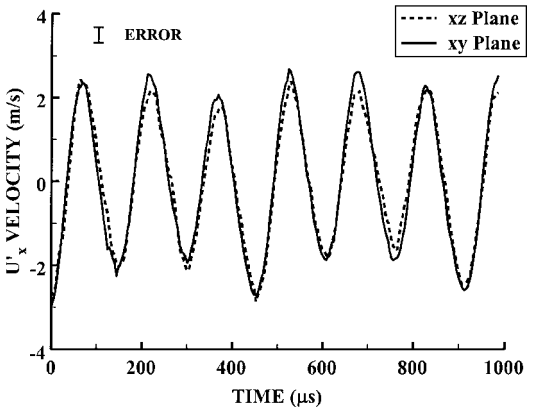

Fig. 8 U'_x velocity comparison, x–y plane vs x–z plane.

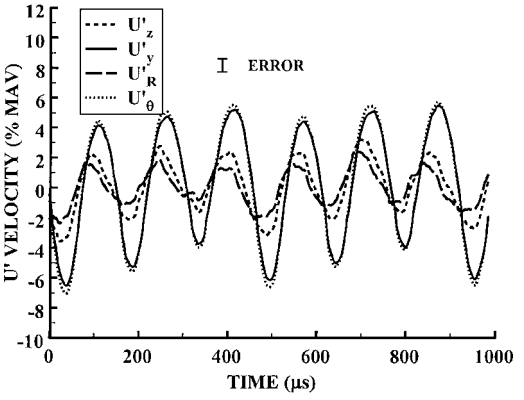

Fig. 9 Coordinate comparison, U'_y vs U'_θ and U'_z vs U'_R.

where Fig. 9 shows the computed U'_θ and U'_R velocities, along with their concomitant U'_y and U'_z velocities, at 13,300 fan rpm, EA 2, vane B, $x/c = 0.3$. From Fig. 9, it is clear that U'_θ and U'_y are nearly identical, whereas U'_R and U'_z are less similar, but agree within the experimental error.[13] The agreement between the two coordinate systems can be attributed to probe positioning. The probe was positioned near $\theta = 90$ deg in the engine cylindrical coordinates; thus, the U_y and U_z directions approximately coincided with the U_θ and U_R directions, as shown in Fig. 4. Because the velocities obtained in the two separate coordinate systems are nearly identical, for the purposes of this paper all results will be given in Cartesian coordinates; however, the results can be interpreted in cylindrical coordinates without error.

Phase Analysis

The phase information obtained from the decomposed velocity data, as exhibited in Table 1, allowed for the construction of disturbance position-vs-phase maps. Figure 10 gives the phase map for the primary-frequency U'_x phase data obtained at the EA 1, vane B location, at 14,375 fan rpm (the phase is adjusted to pass through 0.0 rad at $x/c = 0.0$). Figure 10 also shows a computed phase curve based on the model developed by Fabian and Jumper[11] for upstream-propagating potential disturbances emanating from a non-rotating source. The model equation is given by

$$\varphi = -[2\pi f x/(a - \bar{U}_x)] \tag{3}$$

Comparison of the computed data from Eq. (3) with the measured phase data, as seen in Fig. 10, provides several important results. First, the computed data are aligned in a straight line, indicating propagation in a uniform flow without impediment from other perturbations that may lead to destructive or constructive interaction. Second, the value of the computed data decreases with increasing x/c along a negative slope of $-2\pi f/(a - \bar{U}_x)$, which denotes a

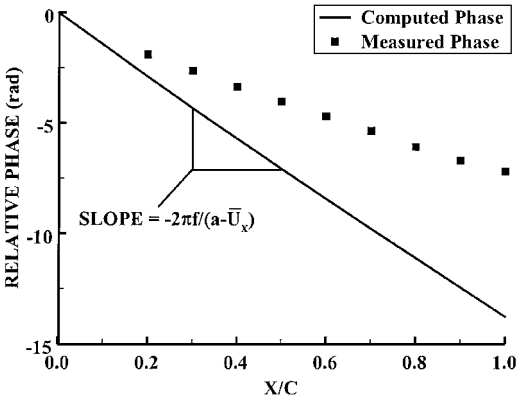

Fig. 10 Non-rotating source model vs measured phase data, 14,375 fan rpm.

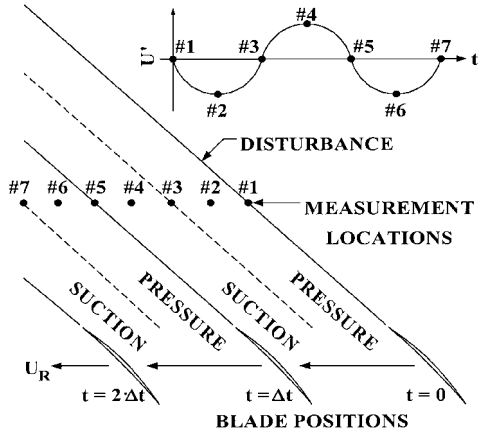

Fig. 11 Streamline measurement of blade disturbances.

potential disturbance propagating directly upstream at the acoustic speed of an axial flow, $a - \bar{U}_x$. Further examination also shows the measured data to be approximately aligned along a straight line, which implies that the measured disturbances traveled in a nearly uniform flowfield. The numerical value of the measured data also decreases with increasing x/c, like the computed data; however, this decline does not occur along the same slope as the computed data. The difference between the two data slopes implies that the measured data did not propagate acoustically. Rather, if the propagation direction were directly upstream, the measured data indicate a propagation faster than the acoustic speed, which is not physically possible because all potential disturbances in a subsonic flow propagate acoustically.[2] Such characteristics were consistent for all of the measured phase data, independent of fan rpm, azimuthal location, or radial position.

Rotating-Source Model

Because the source of the measured disturbances in the F109 was assumed to be the fan, it was necessary to develop a rotating-source model to address the non-physical issues associated with the non-rotating-source model of Eq. (3). The rotating-source model was based on three premises. First, the sinusoidal structure of the measured velocity, as seen in Fig. 7, was assumed due to the X probe measuring the effects of the suction and pressure surfaces of the fan blades. As shown in the rotating reference frame of Fig. 11, velocity peaks were assumed due to the probe measuring the effect of the suction surface of a blade, and velocity troughs were assumed due to the probe measuring the effect of the pressure surface of a blade where the suction surface induced a higher velocity than the corresponding pressure surface.

The second premise assumed that the velocity disturbances, in the inertial reference frame, propagated upstream into the inlet flow along the direction of the rotating-frame streamlines, where the measured mean-inlet flow was almost purely axial. Note that the measured inertial-frame and rotating-frame streamlines were not coincident, as shown in Fig. 12. The rotating-frame streamlines were aligned parallel to the total-velocity vector in the velocity triangle, and the inertial-frame streamlines were axially aligned. Therefore, if the flow was incompressible (in which case disturbance propagation would be instantaneous), a disturbance created by a fan blade would have been measured first at the location axially farthest upstream. The next closest axial location to the fan, along the same engine ray, would have measured the same disturbance at a later time, and so on, with a lag between axial measurements of

$$\Delta t_i = \Delta x / \bar{U}_x \tag{4}$$

Note in Eq. (4) that the disturbance was assumed to move axially along the engine ray at $\bar{U}_x$ toward the fan, covering a distance of Δx between measurement locations, as shown in Fig. 12.

The third premise assumed that, in a compressible flow, elicited disturbances are not felt upstream instantaneously, but rather at a delayed time. The magnitude of this delay is related to the local speed of sound, the axial-flow velocity, and the distance between the observation and emission points. Therefore, with F109 inlet Mach numbers of approximately 0.4, the measured disturbances in the engine had a time delay associated with their measurement, due to flow compressibility. Figure 13 presents an idealized model of the disturbance propagation between a fan blade and the first axial measurement location along an engine ray (located Δx upstream of the fan) in a compressible flow. As depicted in Fig. 13, a fan-induced disturbance, or potential disturbance, was assumed to propagate at the speed of sound along the same rotating-frame

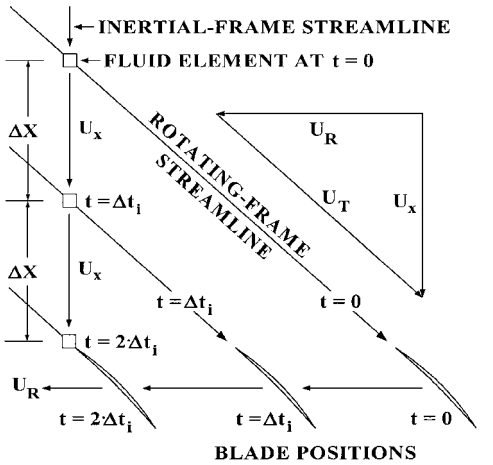

Fig. 12 Incompressible disturbance propagation model.

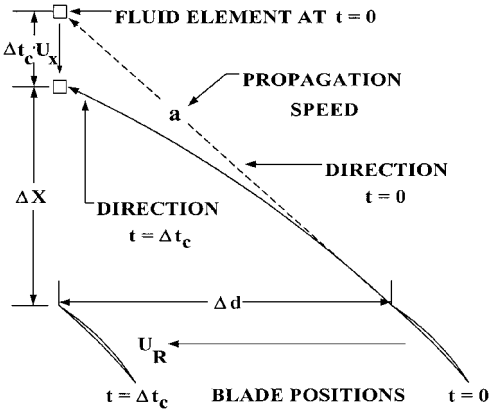

Fig. 13 Compressible disturbance propagation model.

streamline direction shown in Fig. 12, giving a time delay between emission and measurement of

$$\Delta t_c = \left[\sqrt{(\Delta x + \Delta t_c \cdot \bar{U}_x)^2 + \Delta d^2}\right]/a \tag{5}$$

In Eq. (5), the axial propagation distance was modified from Δx by $(\Delta t_c \cdot \bar{U}_x)$, which accounts for the movement of the mean flow toward the fan during the time Δt_c. Solving Eq. (5) for Δt_c then produces the following relation:

$$\Delta t_c = \frac{\Delta x \cdot \bar{U}_x + \sqrt{a^2\Delta x^2 + a^2\Delta d^2 - \bar{U}_x^2\Delta d^2}}{a^2 - \bar{U}_x^2} \tag{6}$$

Finally, when all three premises are combined and the incompressible and compressible effects described by Eqs. (4) and (6) are assumed occur to simultaneously, the phase change in a disturbance moving between two, fixed measurement locations along an engine ray was computed as

$$\Delta\varphi = 2\pi f\,(\Delta t_i - \Delta t_c) \tag{7}$$

Phase Results

The decomposed, primary-frequency phase data for the U_x' velocity, obtained at EA 1, vane B, are given in Figs. 14–16. Figures 14–16 include the computed phase data produced using Eq. (7). Clearly, Figs. 14–16 indicate excellent agreement between the computed and measured phase data, at all three fan rpm (the $x/c = 0.90$ and $x/c = 1.00$ data in Fig. 16 are discussed below). The implications of this phase agreement, given the arguments leading to Eq. (7), suggest that the measured phase data represent upstream-propagating, acoustically radiating potential disturbances, where the disturbances propagate upstream in a helical pattern along the direction of the rotating-frame streamlines.

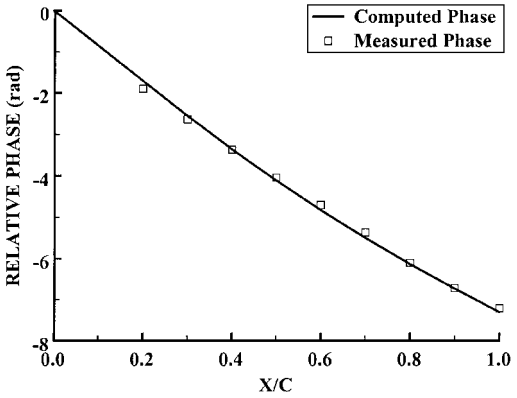

Fig. 14 Rotating-source model vs measured phase data, 14,375 fan rpm.

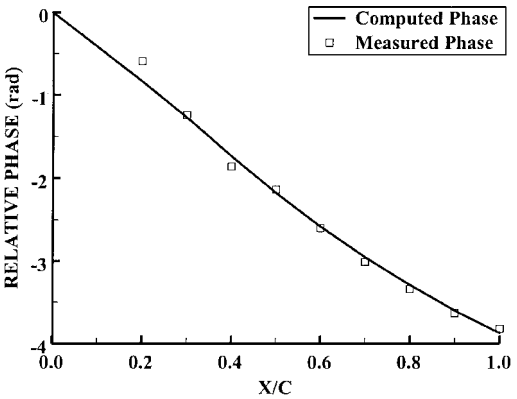

Fig. 15 Rotating-source model vs measured phase data, 13,300 fan rpm.

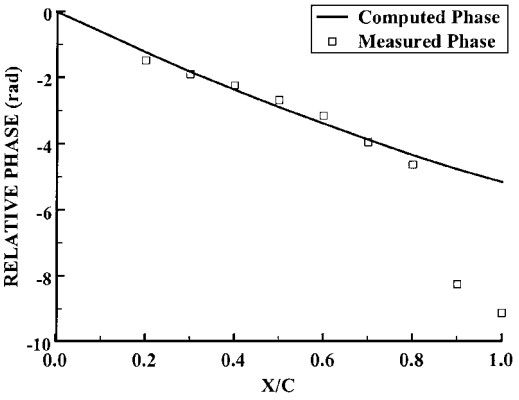

Fig. 16 Rotating-source model vs measured phase data, 12,050 fan rpm.

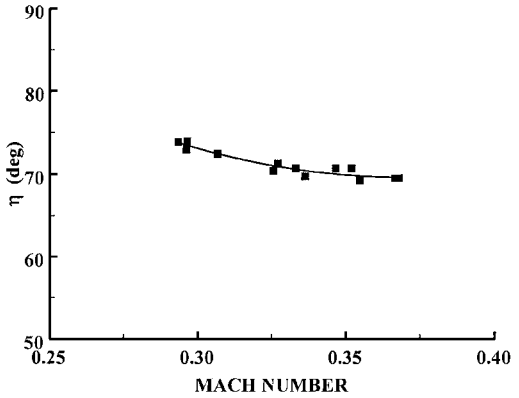

Fig. 17 Disturbance-propagation angle vs F109 average inlet Mach number.

Note that the phase agreement of Figs. 14–16 was achieved through an iterative process. All parameters comprising the disturbance model of Eq. (7) were either measured or known with the exception of Δd, which relates the azimuthal distance traveled by the fan during the time Δt_c. Thus, for each engine run, which allowed for the sequential collection of data along a single engine ray, a single value of Δd was optimized to produce consistent computed and measured phase data. To evaluate the correctness of these iterated values of Δd, the following relation was adopted:

$$\eta = \arctan(\Delta d/\Delta x) \tag{8}$$

Equation (8) relates the angle between the axial distance Δx and the azimuthal distance Δd, as shown in Fig. 13, which provides a direct measure of the disturbance propagation angle. The variation of η with mean inlet Mach number is given in Fig. 17 for each engine run of this study. Note in Fig. 17 that η is approximately constant at 70 deg for Mach numbers above 0.3, but slightly increases for Mach number below 0.3. In fact, the average value of η was 71.2 deg, which is consistent to within approximately 1 deg of the design, F109 total-velocity angle of 70 deg (Ref. 13). Thus, the η values are compatible with the assumed, disturbance propagation direction in the rotating-source model of Eq. (7) and, therefore, provide consistent results.

The iteration of Δd for each individual engine run, rather than a direct application of $\Delta d = \Delta x \cdot \tan(70\ \text{deg})$, was necessary to accommodate differences in engine operating conditions on a run-to-run basis. Because of uncontrollable inlet-air conditions in the engine test cell, the performance of the F109 for each run was unique to its day and time. Thus, the deviation of η from 70 deg at Mach numbers below 0.3 is not surprising given that the phase data could not be normalized with respect to engine operating conditions.

Although not presented here, phase maps similar to Figs. 14–16 were constructed for all fan rpm along each engine ray. Excellent agreement was obtained in these phase maps between the measured and computed phase data at 14,375 and 13,300 fan rpm. The

12,050 rpm data also showed good agreement; however, far from the fan the measured 12,050 rpm data were observed to deviate from the computed data, as shown in Fig. 16. Such deviations may be attributed to low unsteady velocities at the given rpm, producing greater error in the frequency decomposition.

Unsteady Amplitude Results

Figures 18 and 19 show the maximum, peak-to-peak fluctuations for the U'_x and U'_y velocities at EA 1, vanes A and AB, and all three fan rpm, respectively. Peak-to-peak velocity fluctuation is defined as the velocity difference between a peak and trough for a given 200-ensemble signal. Figure 18 shows that very near the fan the maximum peak-to-peak fluctuations in the U'_x velocity reach ~20% of the MAV for 13,300 rpm, whereas at $x/c = 1.0$ the fluctuations fall to less than 2% of the MAV for 12,050 and 13,300 rpm. More important, Fig. 19 shows that very near the fan the maximum peak-to-peak fluctuations in the U'_y velocity (swirl) reach ~50% of the MAV for 13,300 fan rpm; whereas at $x/c = 1.0$, the fluctuations drop to 2–5% of the MAV for both 12,050 and 13,300 fan rpm.

The 13,300 and 12,050 rpm data in Figs. 18 and 19 show similar trends throughout the range of x/c, with an overall decrease in fluctuation magnitude apparent for the 12,050 rpm data. In contrast, both the U'_x and U'_y data at 14,375 rpm show only a small increase in fluctuation magnitude near the fan, with little decay away from the fan. Such behavior suggests the ducted fan to have triggered a cut-on acoustic-propagation mode at 14,375 rpm, where the fan-induced potential disturbances may propagate upstream unattenuated; in fact, analytical duct-acoustics analysis predicts cut-on propagation for the given 14,375 fan rpm conditions.[13]

To further evaluate the large-magnitude velocity fluctuations measured forward of the F109 fan, a computational analysis was performed by Šekularac[14] on the F109 fan geometry and inlet conditions through the use of a compressibility-corrected direct Laplace solver. In this analysis, the potential field both upstream and downstream of an isolated F109 fan stage was computed, revealing that large-magnitude velocity fluctuations exist throughout the upstream field.

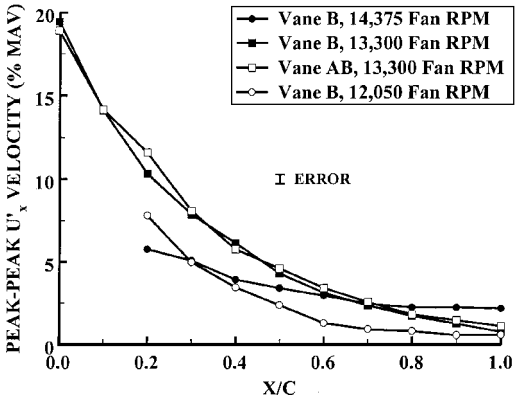

Fig. 18 Peak-to-peak fluctuations in U'_x velocity, EA 1.

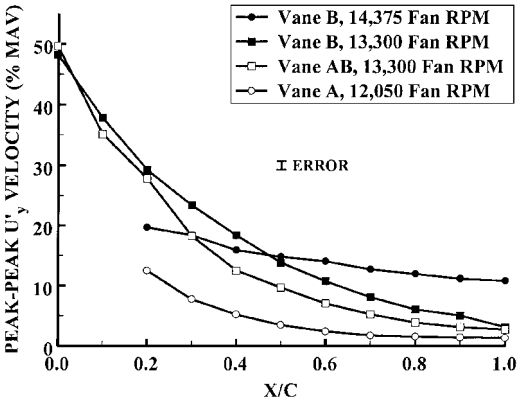

Fig. 19 Peak-to-peak fluctuations in U'_y velocity, EA 1.

The peak-to-peak magnitudes of these upstream velocity variations, in the azimuthal direction, were found to be on the order to 61% of the MAV at locations very near the fan, falling to 0.3% at 1.0 fan-blade chords upstream, while also exhibiting a similar decay rate to that shown in Figs. 18 and 19 (Ref. 14). Thus, these computational results quantitatively agree with the experimentally observed potential field upstream of the F109 fan; providing additional verification of our velocity measurements.

Conclusions

Unsteady, phase-locked velocity measurements were collected upstream of the F109 fan. Phase analysis of the frequency-decomposed measurements suggests that unsteady potential disturbances are elicited by the F109 fan and that they propagate upstream at acoustic speeds in a spiraling helical pattern. These disturbances exhibit large-magnitude velocity fluctuations very near the fan, particularly in the swirl velocity direction (direction normal to an upstream component surface), but decrease in magnitude as they propagate forward; significant flow unsteadiness is observed out to 1.0 fan-blade chords upstream. Computational analysis of the potential field around the F109 fan-blade row was found to exhibit similar magnitude unsteady-velocity disturbances, in the swirl velocity direction, to those measured upstream of the fan.

The existence of large-magnitude potential disturbances propagating upstream of a rotor is notable, particularly when considered in the context of upstream compressor components. Previous investigations have shown upstream-propagating potential disturbances to produce significant unsteady surface-pressure response on upstream blade/vane components.[9–12] However, these previous investigations have either examined supersonic flow conditions in a compressor rig[9,10] or non-rotating forcing in a transonic cascade.[11,12] As such, it remains unclear to what extent the large-magnitude, fan-induced subsonic disturbances measured in the F109 engine would affect the surface-pressure response on an upstream blade/vane component. Moreover, it is unknown how an upstream component would alter the fan-induced potential field. Therefore, although the current paper provides experimental results concerning the propagation characteristics and magnitudes of fan-induced potential disturbances, further investigation is necessary to determine the consequences of these disturbances on the surface-pressure response of an upstream blade/vane component, particularly with regards to component structural HCF failure.

Acknowledgments

This research was jointly sponsored by the Turbine Engine Division of the Aero-Propulsion and Power Directorate at Wright–Patterson Air Force Base, the Notre Dame Department of Aerospace and Mechanical Engineering, the U.S. Air Force Academy Department of Aeronautics, and the NASA Indiana Space Grant Consortium.

References

[1] Thomson, D., "The National High Cycle Fatigue (HCF) Program," *Proceedings of the 3rd National Turbine Engine High Cycle Fatigue Conference*, San Antonio, TX, Feb. 1998.

[2] Fleeter, S., "Forced Response Unsteady Aerodynamic Experiments," AIAA Paper 92-0114, Jan. 1992.

[3] Lewis, J. P., Delaney, R. A., and Hall, K. C., "Numerical Prediction of Turbine Vane-Blade Aerodynamic Interaction," *Journal of Turbomachinery*, Vol. 111, No. 4, 1989, pp. 387–393.

[4] Manwaring, S. R., and Wisler, D. C., "Unsteady Aerodynamics and Gust Response in Compressors and Turbines," American Society of Mechanical Engineers Paper 92-GT-422, June 1992.

[5] Feirerisen, J. M., and Fleeter, S., "Unsteady Potential Effects on Rotor Wake and Stator Unsteady Aerodynamic Response," AIAA Paper 98-3432, July 1998.

[6] Johnston, R., and Fleeter, S., "Time-Resolved Variations of an IGV Flowfield in the Presence of a Rotor Potential Field," AIAA Paper 96-2670, July 1996.

[7] Johnston, R., and Fleeter, S., "Three-Dimensional Time Resolved Measurements of IGV–Rotor Potential Interactions," AIAA Paper 98-3896, July 1998.

[8]Hsu, S. T., and Wo, A. M., "Near-Wake Measurement in a Rotor/Stator Axial Compressor Using Slanted Hot-Wire Technique," *Experiments in Fluids*, Vol. 23, No. 5, 1997, pp. 441–447.

[9]Probasco, D. P., Wolff, J. M., Copenhaver, W. W., and Chriss, R. M., "Unsteady Blade Row Potential Interaction in a Compression Stage," AIAA Paper 97-3285, July 1997.

[10]Probasco, D. P., Wolff, J. M., Copenhaver, W. W., and Chriss, R. M., "Axial Spacing Effects in a Transonic Compressor on the Upstream Vane Loading," AIAA Paper 98-3431, July 1998.

[11]Fabian, M. K., and Jumper, E. J., "Rearward Forcing of an Unsteady Compressible Cascade," *Journal of Propulsion and Power*, Vol. 15, No. 1, 1999, pp. 23–30.

[12]Fabian, M. K., Falk, E. A., and Jumper, E. J., "Upstream-Propagating Potential Disturbances Interacting with a Compressible Cascade," *Journal of Propulsion and Power* (to be published).

[13]Falk, E. A., "An Experimental Investigation of Aerodynamic Forcing in the F109 Turbofan Engine Compressor," Ph.D. Dissertation, Dept. of Aerospace and Mechanical Engineering, Univ. of Notre Dame, Notre Dame, IN, May 2000.

[14]Šekularac, A., "Potential-Field Disturbances in a Loaded Cascade," M.S. Thesis, Dept. of Aerospace and Mechanical Engineering, Univ. of Notre Dame, Notre Dame, IN, Aug. 2000.